

Article

A Compact Electromagnetic Dual Actuation Positioning System with a 10 mm Range and Nanometer Resolution

Bimal Jeet Goteea, Qianjun Zhang and Wei Dong *

State Key Laboratory of Robotics and Systems, Harbin Institute of Technology, Harbin 150001, China

* Correspondence: dongwei@hit.edu.cn

Abstract: In this manuscript, a compact electromagnetic dual actuation positioning system (CEDAPS) based on the Lorentz force principle that features a 10 mm range and nanometer-scale resolution with flexure guides is presented. Firstly, the stiffness of the flexure mechanism is modelled. Secondly, based on it, the primary coil is designed, and from its performance, a suitable secondary coil is made to compensate for the deficiency of the primary actuation subsystem. The characteristics of the forces generated by these coils are also evaluated by an electromagnetic FEA simulation. Thirdly, a control scheme is presented that combines the performances of these two actuators, and finally, a prototype is fabricated to evaluate the performance. The results show a 10 nm resolution for a 10 mm (± 5 mm) stroke with low sub-micron sinusoidal tracking errors and nanometer accuracy for step tracking under the proposed control scheme. The thermal properties of the system are also presented.

Keywords: electromagnetic actuator; flexure guide; electromagnetic force simulation; macro-micro actuation; nanopositioning stage



Citation: Goteea, B.J.; Zhang, Q.; Dong, W. A Compact Electromagnetic Dual Actuation Positioning System with a 10 mm Range and Nanometer Resolution. *Actuators* **2023**, *12*, 132. <https://doi.org/10.3390/act12030132>

Academic Editors: Tao Chen, Minglu Zhu and Haidong He

Received: 4 February 2023

Revised: 10 March 2023

Accepted: 11 March 2023

Published: 21 March 2023



Copyright: © 2023 by the authors. Licensee MDPI, Basel, Switzerland. This article is an open access article distributed under the terms and conditions of the Creative Commons Attribution (CC BY) license (<https://creativecommons.org/licenses/by/4.0/>).

1. Introduction

Electromagnetic actuators usually operate under the Lorentz force principle and are often employed in a moving coil arrangement. These have as their main advantage non-contacting moving parts and thus offer desirable properties for precision positioning, such as theoretically infinite resolution with cog-free and backlash-free motions. A common example of this actuation scheme is the voice coil motor (VCM). On the downside, precision positioning platforms employing such actuators can be adversely affected by the heat generated by the coil [1,2]. There are also performance tradeoffs to be made, as described in [3]. On the control side, nanopositioning systems pose considerable challenges as described in [4]. The performance also depends highly on the skills of the experimenter, the hardware setup, the type of drives, the controller, and the positioning sensor used [5].

For a positioning stage, an actuator alone is not sufficient, and some form of the guideway is required to constrain motion along a predefined axis. For contact-type linear bearings over small displacements, the stick-slip phenomenon becomes dominant and the frictional forces become highly non-linear [6–9] which makes precision positioning problematic. These can be overcome with non-contact guideways such as magnetic levitation [10–12] and aerostatic bearings [13,14]. However, these are not only voluminous and costly, but they also require additional control as they exhibit multiple degrees of freedom. To rectify these, flexure mechanisms are used, as they are relatively cheaper to manufacture and offer repeatable backlash-free and friction-free motions with zero maintenance and long service life as long as the material with which they are made stays within its elastic limit and the stresses are kept below the fatigue point of the material [15]. Recently, the flexure mechanism has been integrated with the electromagnetic actuator for the millimeter range with nanometer resolution, as in [16,17].

With recent developments in various key sectors, there is a need for an actuator that can be used for embryonic and cell manipulations as in [1], a precision XY positioning

platform with a 10 mm range for biological sample manipulation as in [18], nanometer UV imprinting as in [19], micro-assembly as in [20] and optical alignment [21], amongst other applications. All these require a range of about 10 mm and a resolution better than 50 nm with the additional requirement of not producing excessive heat, which is detrimental to the object they need to position.

For (relatively) long-range and high resolution, usually, a single actuator positioning stage will not satisfactorily meet these two demands simultaneously due to hardware and controller limitations, amongst others. One solution for reconciling fine resolution over a long range is to use a dual actuator stage that consists of a coarse (macro) actuator which does the long-range positioning with a coarser accuracy and a shorter range. However, the finer resolution (micro) actuator that corrects the positioning error to produce a more precise positioning. Traditionally, the micro-positioning stage is attached at the end of the macro-positioning stage serially. This is widely used, for example, in the computer magnetic storage sector, where most mechanical hard disk drives use a rotary VCM for long-range positioning and a Pb-Zr-Ti (PZT) actuator, attached at the end of the positioning arm, for the final positioning of the read/write head [22,23]. This concept is now also widely adopted for 1-DOF positioning platforms [24–27] as well as for multi-DOF platforms [11,28].

However, the use of a PZT actuator is not ideal as the actuation system becomes heterogeneous, where the electromagnetic actuator is usually driven at a low voltage and high currents while the PZT actuator is usually driven at a high voltage and relatively low currents. Additionally, the control of PZT actuators is difficult as they suffer from complex hysteresis [29]. Consequently, electromagnetic actuators are now being used for both positioning stages. Examples of such stages include the use of a linear motor (long range) with a VCM (short range) [30], a pneumatic actuator and VCM [31] and a dual VCM set-up, amongst others. However, these tend to be separate positioning stages connected serially, resulting in the main (coarse) actuator having to bear the additional load and motion dynamics of the fine actuator positioning stage. When the actuators are connected back-to-back on the same positioning stage, this results in inter-actuator motion disturbance. This is because electromagnetic actuators rely on coils and magnets, which have significant weight and bulk. Additionally, there are interactions between the resulting magnetic fields that distort the force characteristics of the two actuators due to magnetic attraction and repulsion. These factors pose significant control challenges for such a positioning stage as described [32] for a dual VCM setup. Furthermore, extra care must be taken to route the usually thick connecting wires, which need to carry large currents at low voltages to avoid wire-induced disturbances. Another possible solution is to wind both coils on the same bobbin, as in [33] to use only one positioning stage. Even though each coil is wound on the same bobbin, each has its magnetic circuit. However, such a design suffers from two main drawbacks: 1. the range is limited by the travel distance of the microactuator as for electromagnetic actuators employing the Lorentz force principle, to produce any appreciable force, the coil must be in the air gap and experience as much of a uniform magnetic field as possible, and 2. magnetic interference occurs when the magnetic fields generated by the coils interact with each other. Consequently, their specialized actuator has a range of less than 40 μm and is used for specialized semiconductor fabrication testing.

The problem of serially connected positioning stages can be addressed by using parallelly connected positioning stages. An example of such a positioning stage is [34], where two individual Halbach-type VCMs were used in a parallel configuration. The advantage of this design is that the two stages are decoupled, and the two actuators can operate independently from one another. Other works, based on the same principle, but with different actuators, include [35–37] amongst others. However, these still rely on two separate mechanical positioning stages.

In this manuscript, we propose a homogenous 10 mm-range and high-resolution dual actuator stage electromagnetic actuator based on the macro-micro principle, where the two actuators are in parallel and only one positioning stage is used. This configuration combines the advantages of dual positioning stages employing electromagnetic actuators

while overcoming the disadvantages of having serially connected stages and actuators. The microactuator shares the same bobbin and air gap as the macro actuator and can thus travel over the full range. Additionally, the weight of the microactuator is minimal as it consists only of a much smaller coil and consequently does not affect the natural frequency of the positioning stage which, is dependent on stiffness and mass. The concept is validated with the fabrication of a 1D prototype positioning platform. The resulting positioning stage has a motion range of ± 5 mm and a resolution of 10 nm. On the performance side, there is a significant reduction in tracking and positioning errors, which are in the low submicron range. Additionally, the thermal effect is evaluated, and the temperature rise after one hour is less than 2.4 °C. The concept of the micro-coil can be retrofitted into existing positioning stages employing the VCM without having to redesign the positioning stage to accommodate an external microactuator. The principle can also be extended to other electromagnetic actuators.

The rest of the paper is as follows: Section 2 covers the design of the flexures, the macro and micro coils, and the assembly, together with an electromagnetic simulation of the generated forces. Next in Section 3, the characteristics of the coil, the current drive, and the controller are presented. In Section 4, the experimental verification of the proposed nanopositioning system is presented, the results are discussed in Section 5 and finally, a conclusion is presented in Section 6.

2. Mechanical and Actuator Design

2.1. Design of the Flexure Mechanism

The positioning system is designed to have a range of ± 5 mm while also being compact. Consequently, a guiding mechanism based on three multiple compound parallelogram flexures (MCPFs) was designed based on the previous works [38,39].

Figure 1 shows the assembly, with motion directed along the x -axis, and one flexure unit with associated dimensions, which is used to derive the stiffness and the force required for an arbitrary displacement. Using the fix-sliding model, the flexure is decomposed into six blades, each with one end fixed and the other end free to translate. Each blade is subjected to a combined moment, M , an axial reaction force, R , and a force, F , when a force F_x is applied to the primary side. This results in a statically indeterminate beam, and after applying the appropriate boundary conditions, the resulting one-sided displacement, Δx , is given by:

$$\Delta x = 5\delta x + \delta x_1 \quad (1)$$

where δx is the displacement for the blades having length l , and δx_1 is that for the blade of length l_1 . The stiffness, K , can be written as:

$$K = \frac{2F}{\Delta x} \quad (2)$$

with $F_x = \frac{F}{2}$, $\delta x = \frac{Fl^3}{12EI}$, $\delta x_1 = \frac{Fl_1^3}{12EI}$, $I = \frac{bh^3}{12}$. Substituting these gives K :

$$K = \frac{2Ebh^3}{(5l^3 + l_1^3)} \quad (3)$$

in terms of the material and physical properties of the flexure, where E is Young's modulus in GPa, b is the width, h is the thickness, and l and l_1 are the lengths of the flexure blades as per Figure 1b, with all the lengths in meters.

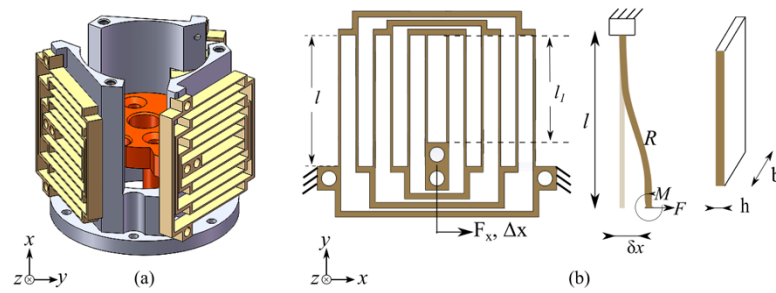


Figure 1. (a) Projected view of the motion platform with 3 flexures connected in parallel. 1. Flexure unit, 2. Motion platform (head), and 3. Flexure holder; (b) Design of one flexure unit.

The flexures and head are made of aluminum 2A21, whose properties are given in Table 1. Based on the expected force of the actuator, the desired stroke, and compactness, the parameters for the flexure were designed as follows: $h = 0.4$, $b = 4$, $l = 22$, and $l_1 = 18$ with all units in mm. The calculated stiffness of one flexure is 612 N/m, that of the assembly is 1836 N/m (612×3) and that according to FEA is 1781 N/m, which corresponds to a deviation of 3%. The maximum von Mises stress in the flexures, according to the FEA simulation, is 158.4 MPa, which gives the assembly a safety factor of 2.05.

Table 1. Mechanical properties of aluminum 2A21.

Property	Value
Tensile strength (MPa)	470
0.2 % yield strength (MPa)	325
Young's modulus (GPa)	70.6
Poisson's ratio	0.33
Density (kg/m^3)	2780

2.2. Design of the Macro Coil

A contactless electromagnetic actuation scheme was chosen as such actuators usually do not have a preferred position and are free from contact between the moving and stationary parts, making them ideal for precision positioning applications. We started by finding the number of turns required for the coil to produce the desired force, and from this, a suitable coil is fabricated based on the physical constraints imposed by the air gap and bobbin. From there, the open loop performance of the actuator is determined based on the characteristics of the drive system.

The base design objective is to have a force constant of at least 10 N/A as a 5-mm displacement requires an 8.9 N force. For ease of realization, an existing stator with radial magnetization was reused. The averaged magnetic field at the center of the air gap was measured to be 0.27 T and from the Lorentz Force equation:

$$F = i \int dL \times B \quad (4)$$

which can be reformulated as:

$$F = BIlN \quad (5)$$

where F is the generated force in N, B is the magnetic field in T, l is the average circumference of the coil (30.5 mm) in m, and N is the number of turns, N is calculated to be 393 turns. The number of turns was increased by 20% to ensure that it has enough force to accelerate the moving parts as well as displace the flexure mechanism, and most importantly, to keep the current required for maximum displacement below 1 A to minimize the heat generated by Joule's heating. These 480 turns give the macro coil an indicative force constant of 12.6 N/A.

For a hexagonal winding pattern, the height, H , of an N -layer coil is given by:

$$H = d + (N - 1)0.866d \quad (6)$$

where d is the diameter of the wire. The desired height to allow sufficient clearance between the top of the micro-coil and the magnets is 1.254 mm. To this end, 0.3 mm enamel copper wire with an external diameter of 0.4 mm was used. The maximum allowable length of the coil is 51 mm if it is to remain in the air gap over the whole ± 5 mm stroke. The coil will have 3 layers if filled end to end. Since an even number of layers is preferred as it allows the wire to enter and exit on the same side, a 4-layer coil with each layer having 120 turns was selected. There is, however, enough space for 170 turns per layer, but this would unnecessarily increase the motional mass, which in turn would reduce the natural frequency of the CEDAPS. Given the resistivity of copper, the dc resistance, R , of the macro coil is calculated to be 11.7 Ω from:

$$R = \rho l_c / A \quad (7)$$

where ρ is the electrical resistivity of copper in Ωm , l_c is the total length of the coil in m, and A is the cross-sectional area of the copper wire used in m^2 . The maximum input dc voltage at which the linear current drives can operate is 48 V, and they have an internal voltage drop of 8 V. This should allow the coil to be driven with a peak current of 3.4 A for brief moments.

The open loop resolution for the displacement of the system when driven by the macro coil can be calculated. The macro coil will produce a force, F , based on the current i applied to it and based on its force constant K_f as:

$$F = iK_f \quad (8)$$

This force will cause a displacement, x , when applied to the flexures with stiffness, K :

$$iK_f = Kx \quad (9)$$

The minimum voltage, V_{\min} that the digital-to-analog converter (DAC) can produce is:

$$V_{\min} = \frac{1}{2^{N_{\text{bits}}-1}} V_{DAC} \quad (10)$$

where N_{bits} is the resolution of the DAC in bits and V_{DAC} is the half-range voltage of the dipolar DAC. This is also equivalent to the voltage per DAC least significant bit (LSB). And the corresponding minimum current, I_{\min} is as follows:

$$I_{\min} = V_{\min} \times T \quad (11)$$

where T is the transconductance of the linear current drive in A/V. With this minimum current, the minimum displacement X_{\min} can be calculated as:

$$X_{\min} = \left(\frac{V_{DAC}TK_f}{2^{N_{\text{bits}}-1}K} \right) \quad (12)$$

2.3. Addressing the Limitation of Positioning with the Macro Coil

In this system, the DAC has a resolution of 16 bits and produces a bipolar output of ± 10 V. The linear current drive for the macro coil has a transconductance of 0.4 A/V and requires a drive voltage of ± 10 V. Given that the flexure has a theoretical (FEA) stiffness of 1781 N/m and the indicative force constant of the macro coil is 12.6 N/A, the open loop resolution is 860 nm. The closed loop resolution will be higher, but it will still not be able to reach the 10 nm range.

There are four ways to increase the resolution of the platform. One is to simply use a DAC with a higher resolution, like 18 or 20 bits. On the practical side, this is not ideal for several reasons: 1. As the number of bits increases, the integral non-linearity (INL) noise, which is the maximum deviation of the actual input-output characteristics from the ideal transfer characteristics, and the differential non-linearity (DNL) noise, which is the difference between two successive voltage levels that a DAC produces, also increase, and this noise can be as high as 4 LSBs depending on the chip manufacturer. 2. The voltage drop across an electrical wire connecting the output of the DAC chip to the current drive, including the connectors, is likely to be too high for such low voltages. This would not have been a problem if these two were mounted in close proximity on the same PCB with proper shielding and impedance matching. 3. The signal-to-noise ratio is not high enough. The LSB from the 20-bit ± 10 V DAC results in a voltage of only $19 \mu\text{V}$. Additionally, the linear dc power supply used has about 70 mV of noise, which fluctuates with the current being drawn and also with the temperature of the power transistors. The DAC circuit and the analog comparators in the current drive have precision voltage references built into them to maintain adequate operation. The $19 \mu\text{V}$ might simply be below the detectable input voltage of the linear current drive. 4. Additionally, the current drive will not be able to reproduce this $7.63 \mu\text{A}$ current reliably as the voltage drop required to generate it will be simply too high for the linear current drive with dissipative realization. This voltage drop, V_{drop} is given by:

$$V_{drop} = (V_s - V_i) - (I_{coil} \times R_{coil}) \quad (13)$$

where V_s is the supply voltage, V_i is the internal voltage drop for the current drive, which is 8 V for this current drive, I_{coil} is the current flowing into the coil in A, and R_{coil} is the resistance of the coil in Ω . In this case, it is 39.99 V for a 48 V supply. This can be implemented if a dedicated low-current amplifier with a low supply voltage is used, but not with an industrial current amplifier capable of 8 A. Second, this problem can also be addressed by selectively switching in a resistive dropper depending on the desired resolution, as in [40]. However, in this application context, switching in and out a resistor every time a different resolution is required is not feasible, especially for tracking dynamic trajectories. The third solution is to use a PZT as a microactuator in a macro-micro configuration. However, these suffer from hysteresis, and they cannot be mounted directly, as some form of supporting platform is required which will add to the motional mass and consequently reduce the natural frequency of the platform. The fourth and selected solution is to use the principle of superposition for forces and to wind a micro coil on top of the macro coil to generate the required corrective forces. This does not require additional external space or a redesign of the mechanism.

2.4. Design of the Micro Coil

The micro coil is designed based on a minimum desired open loop resolution of 20 nm, as the sensor used has a 10 nm resolution. The coil will be driven with a linear current drive having a transconductance of 0.2 A/V with a ± 10 V 16-bit DAC output. Based on the stiffness of the flexure, this 20 nm displacement requires a force of $35 \mu\text{N}$ which corresponds to a K_f of 0.57 N/A. This can be obtained from Equation (12). Given the average magnetic field strength of the air gap and the outer diameter of the macro coil, the micro-coil is to have 21.83 turns, based on Equation (5). 20-turns were chosen and it should yield a resolution better than 10 nm in a close loop. On its own and under ideal conditions, the micro-coil should provide a stroke of $\pm 651 \mu\text{m}$ which ought to be sufficient to correct most positioning errors due to the macro coil. Due to space constraints in the air gap, the micro-coil is wound with 0.27 mm enamel copper wire. From Equation (7), the dc resistance of the micro-coil is calculated to be 0.61Ω and consequently, a 4Ω 50 W power resistor was added in series to increase the voltage drop to keep the linear current drive in its safe operating area (SOA). The supply voltage to the micro-coil current drive is set to 20 V, which should reduce the heat generated by the power electronics by 17% over a standard 24 V supply while still being able to supply a peak current of 2.6 A.

2.5. Electromagnetic Force Simulation for the Coils

A 3D magnetostatic electromagnetic simulation of the forces generated by the macro and micro coils was performed because the performance of the positioning system directly depends on these forces. A 2D simulation is computationally faster, but it cannot fully capture the magnetic field created by the 6 arc-shaped magnets, which would be represented by one solid hollow cylinder, resulting in a much higher generated force. The simulation results are shown in Figure 2a for the macro coil and Figure 2b for the micro coil, respectively, when excited with ± 0.5 A, ± 1 A, ± 2 A and ± 3 A (for macro coil only). The coil was modelled with copper, the bobbin with aluminum 6061, the motor case, back plate, and center pole were modelled with carbon steel 1020, and the magnets were modelled with NbFeB 42. These are standard materials provided by the electromagnetic simulation software. The virtual work and Lorentz force methods yielded identical results. The simulated averaged force constant for the macro coil is 12.4 N/A and 0.56 N/A for the micro coil. The important point to note is that the pushing and pulling forces are not equal and they vary with the stroke. This is because this stator uses a center pole, which forms a return path for the magnetic field and also because the back plate attracts the magnetic field generated by the coils. Also, it is worth noticing that as the current increases, the gap between the pushing and pulling forces widens, and the shape of the force curves changes as the stator saturates due to the magnetic field created by the coil. The magnetic fields generated when 1 A of current flows through the two coils are shown in Figure 2c, along with the optimal placement of the micro-coil for the least magnetic interference by the macro coil.

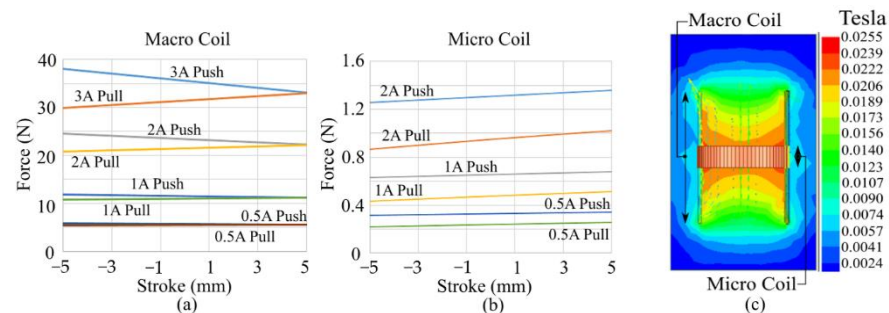


Figure 2. The simulated force generated by various currents at different strokes by (a) Macro; (b) Micro coil; (c) Magnetic field distribution around the coils when 1 A of current flows through each.

2.6. Assembly

The assembly is shown in Figure 3. Except for the flexures, the remaining parts of the assembly were fabricated out of aluminum 6061 for rigidity. Non-magnetic fasteners were used to minimize magnetic interferences. One often overlooked factor is the damping coefficient, c , which depends primarily on the induced Eddy currents flowing in the aluminum bobbin and the coils. However, it also depends on the amount of air trapped in the gap between the inner surface of the bobbin and the center pole and back plate. As the bobbin moves, it either compresses or expands the air. This phenomenon becomes more prominent in high-speed reciprocating (sinusoidal) motions, and sufficient clearance must be provided to allow the air to escape. Additionally, the head has cut-in slots to allow the exit of the wires while also preventing them from bending excessively to reduce wire-induced disturbances. To this end, multistrand copper wires with very supple silicon insulation were used. A non-contact linear incremental encoder was employed for position sensing as it has many advantages for industrial applications, such as robustness, a relatively simple setup, and excellent noise immunity when properly terminated.

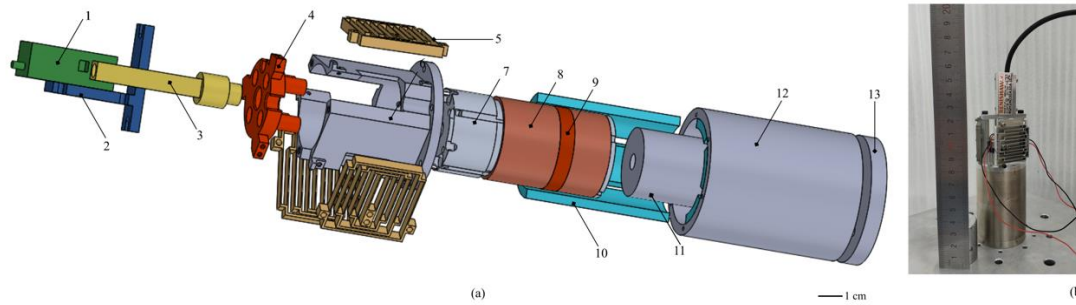


Figure 3. (a) Exploded view of the proposed positioning stage. 1. Linear incremental encoder, 2. Encoder holder, 3. Encoder ruler holder, 4. Motion platform (head), 5. Flexure x 3, 6. Flexure assembly holder, 7. Bobbin, 8. Macro coil, 9. Micro coil, 10. Arc-shaped magnet x 6, 11. Center pole, 12. Motor case, 13. Back plate; (b) The fabricated positioning system.

An FEA was conducted to determine the vibration modes of the CEDAPS. The first 5 vibration modes occur at 23.37 Hz, 117.47 Hz, 122.14 Hz, 203.5 Hz, and 203.5 Hz, respectively. Since this motion platform is used for nanopositioning and also due to actuator performance, only the first two vibration modes, as shown in Figure 4a,b, are of interest. It can be seen that up to the second mode, the vibrations are mostly contained along the axis of motion (x), making it usable above the first mode.

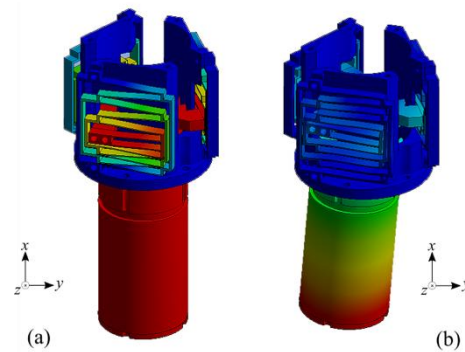


Figure 4. (a) First vibration mode at 23.37 Hz; (b) Second vibration mode at 117.47 Hz.

The measured stiffness is 1650 N/m, which is within 8% of the FEA value.

3. Electrical Parameters of the Coils, Current Drive Non-Linearities, Actual Force Constants and Controller

3.1. Electrical Parameters of the Coils

The macro coil has 480 turns with a dc resistance (R) of 11.9 Ω and an inductance (L) of 1.060 mH when measured with a 4-wire LCR meter at 1 kHz, and the micro coil has 20 turns with a dc resistance of 0.9 Ω (without the 4 Ω 50 W power resistor) and an inductance of 16.5 μ H. The inductances are measured at zero displacements (midstroke) and they vary along the stroke due primarily to changes in the magnetic field at the center pole. The time constant (L/R) for the macro coil is 89.1 μ s and 18.3 μ s for the micro coil which enables the latter to respond about 4.9x faster to changes in current. The cutoff frequency, F_c :

$$F_c = \frac{R}{(2\pi L)} \quad (14)$$

of the macro coil is 1.787 kHz, while that of the micro-coil is 8.686 kHz. The current drive has a 5 kHz bandwidth. With these, the sampling and actuation frequencies of the control system are set to 1 kHz. Crosstalk between the two coils can be ignored as the actuation frequencies are well below radio frequencies (30 kHz to 6 GHz), the inductances are relatively small, and the aluminum bobbin is diamagnetic.

3.2. Current Drive

The ideal transconductance of the current drive for the macro coil is 0.4 A/V and 0.2 A/V for the micro coil. However, the current drives exhibit a zero offset error and a deviation from ideal behavior. A comprehensive explanation for such types of deviations can be found in [41]. The corrected relationships for the macro and micro coil current drives are respectively:

$$I_{macro} = 0.4318V - 0.0047 \quad (15)$$

$$I_{micro} = 0.1989V - 0.0174 \quad (16)$$

3.3. Force Constant

The pushing and pulling force constants were obtained by measuring the generated force at a particular stroke while varying the applied current. The slope of the force-current curve at that stroke is then used to determine the force constant at that point. By so doing, non-linearity due to magnetic saturation is taken into consideration as opposed to just measuring the force generated at 1 A. These slopes are then interpolated to find the proper force constant at any point along the stroke based on whether a pushing or pulling force is required. A T098H0-10V bridge amplifier with a T310-50N sensor having a measurement range of 50 N with a 0.01 N resolution from Right Co. Ltd (Changzhou, China). was used to measure the generated force. The resulting force constants for the macro and micro coils are shown in Figure 5. The average force constant for the macro coil is 13.5 N/A, while that for the micro coil is 0.5 N/A. The actual force generated by the actuator is higher than calculated because the magnetic field inside the air gap is not constant due to the fringing caused by the 6-arc-shaped magnets and the exact materials used for the construction of the stator are unknown. Also, small assembly flaws can result in the magnets not all being at the same distance from the center pole, and this can significantly affect the resulting magnetic field in the air gap. Another way of obtaining only the parts of the force curves used, which does not require the use of a force sensor, is to use the stiffness of the flexure to access the force produced by measuring the ensuing displacement when known currents are randomly applied to the coils in an open loop. The data gathered can then be converted into force per ampere, and the force curve can then be determined by running a linear regression algorithm after removing spurious data points due to environmental noise affecting the displacement. The data points are shown as dots in Figure 5 and they line up with the force curve obtained by the force sensor.

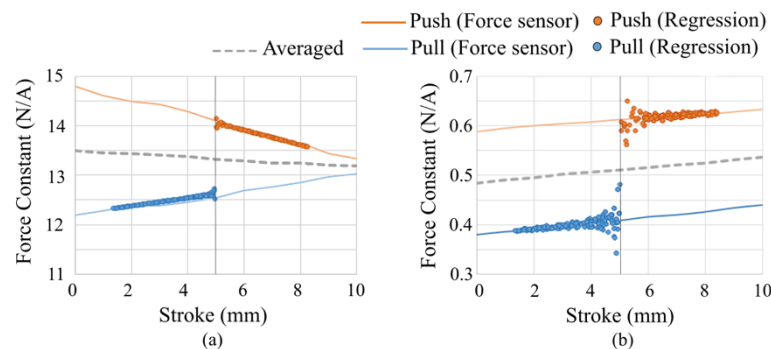


Figure 5. Force constant (a) Macro coil; (b) Micro coil.

The importance of characterizing the forces is shown in Figure 6 for tracking a 2.5 mm 1 Hz sinusoidal reference with the controller in Section 3.4 with the macro plus micro coil actuation. The tracking root mean square error (RMSE) without the Force-to-Current blocks, (w.r.t. Section 3.4) and using the averaged K_f of 13.5 N/A for the macro coil and 0.5 N/A for the micro coil, is 8.01 μm and 24.88 μm for the maximum absolute error (MAXE) as opposed to 0.058 μm and 0.136 μm respectively, when these blocks are in place. These

differences are significant. The shape of the error curve without them can be contrasted with Figure 10d.

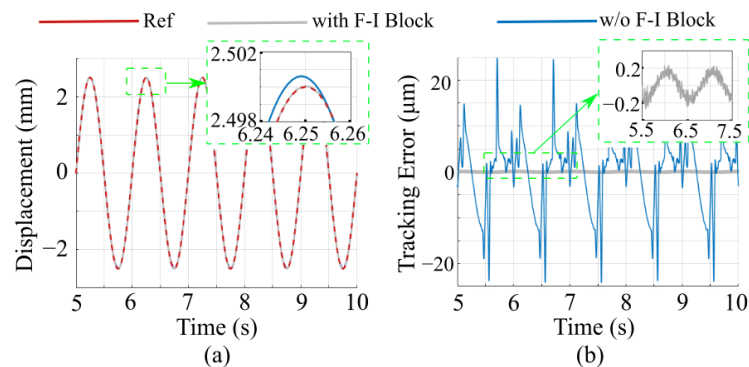


Figure 6. Tracking of 2.5 mm 1 Hz sinusoidal trajectory with and without the Force-to-Current (F-I) blocks. (a) Tracking performance; (b) Error.

3.4. Controller

On the control side, the bulk of the positioning is done with the macro coil, which is controlled with a feed-forward (FF) and PID feedback (FB) position controller. These controllers produce a force command that is to be reproduced by the macro coil to position the platform. As shown in Section 3.3, the force generated by the VCM varies along the stroke and exhibits hysteresis. This effect is countered using a Force-to-Current block. The current drives also deviate from ideal transconductance behavior, as shown in Section 3.2 and this is rectified with a Current-to-Drive-Voltage block. These two aforementioned blocks are the inverse models of their corresponding hardware, and with these blocks in place, the system becomes closer to being linear time-invariant (LTI), which ensures better performance. The 16-bit DAC converts the control signal into a drive voltage, which is fed to the linear current drive (Trust Automation TA115), which is powered by a linear DC power supply (UNI-T 3050A). These feed the coil with the commanded current, which is then converted into a force by the magnetic circuit of the stator. The resulting displacement is measured with a linear incremental encoder (Renishaw RGH24O30A0A), which has been properly terminated at the data acquisition card (NI 6229) to eliminate noise in the form of signal reflection. The micro coil controller has the task of eliminating the discrepancies, which the macro coil controller cannot. The commanded force for the macro coil is compared with the force being generated at the platform through the P^{-1} block, which is similar to the feedforward block used for the macro coil. This discrepancy is then fed into a PI force feedback controller to drive the micro coil. Figure 7 shows a simplified schematic of the proposed controller. The disturbances in the system can be broadly described as d_1 and d_5 , DAC quantization error; d_2 and d_6 , electrical noise from the power supply and Johnson noise in the linear current drives; d_3 and d_7 , parameter uncertainties in current to force conversion and d_4 , any mechanical disturbance on the system such as unwarranted environmental vibrations and wire induced disturbances.

The feedback control for the micro coil may seem similar to a disturbance observer (DOB), but the main difference is that no filter (Q) is used, and the disturbance is fed to a PI force controller. This is done for two reasons: 1. the Q filter is difficult to design for a non-minimal phase system [42]; and 2. the filtering of the signal makes the high-frequency noise that needs to be suppressed by the micro coil be suppressed prematurely, worsening the performance. This is because the Q filter acts as a low-pass filter.

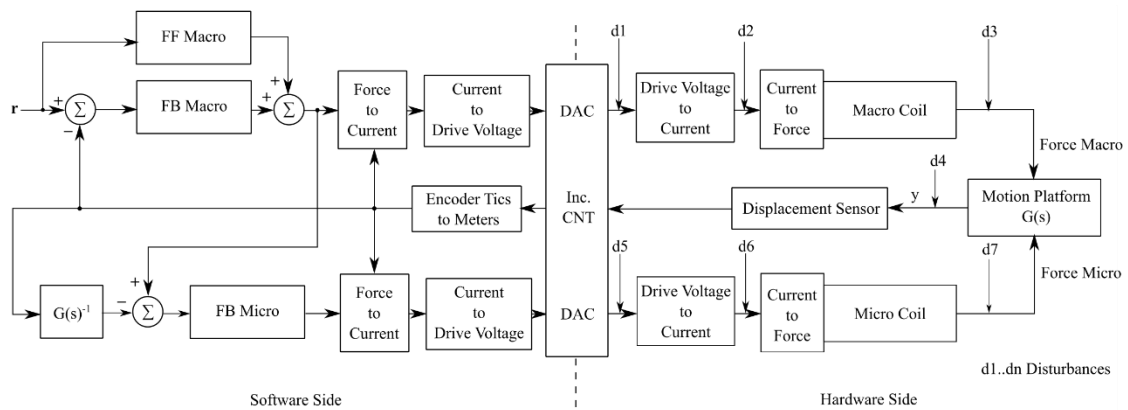


Figure 7. Simplified schematic of the controller.

The discretized version of the derivatives for calculating the feed-forward control ($F_{plant}(k)$) and the inverse of the plant ($G(k)^{-1}$) and standard ideal algorithm (ISA) PIDs ($u_{pid}(k)$) are used in the implementation, and their Z transforms are given as:

$$u_{pid}(k) = K_p \left(1 + K_i T_s \frac{1}{z-1} + K_d \frac{N}{1 + N \cdot T_s \frac{1}{z-1}} \right) e_k \tag{17}$$

and

$$F_{plant}(k), P^{-1}(k) = \left(m \frac{(z-2)}{T_s Z} + c \frac{(z-1)}{T_s Z} + k_s \right) x_k \tag{18}$$

where e_k is the tracking error, K_p , K_i , and K_d are the PID coefficients, N is the filter coefficient, T_s is the sampling time of the controller, and subscript k is the sample number. m , c , and k_s are the mass, the damping coefficient, and the stiffness, respectively.

The following PID values were used for all the experiments unless stated otherwise: for the macro coil, $K_{p_M} = 15$, $K_{i_M} = 11,000$, and $K_{d_M} = 1$ and $K_{p_m} = 2$, $K_{i_m} = 18$, and $K_{d_m} = 0$ for the micro coil.

4. Experimental Results

4.1. System Identification

With the proper compensation of the non-ideal behaviors, the transfer function of the CEDAPS was identified concerning an applied force. The system could have been identified with current, but it would have included the actuating coil force constant, which, as shown previously, varies along the stroke. The dynamics can be modelled as a mass-spring-damper system:

$$F = m\ddot{x} + c\dot{x} + k_s x \tag{19}$$

where F is the applied force, which is generated by the actuator x , \dot{x} , and \ddot{x} are the displacement, velocity, and acceleration, respectively, m is the motional mass, c is the coefficient of damping and k_s is the stiffness of the flexure mechanism. A force-swept sine wave ranging from 0.1 to 100 Hz with an amplitude of 0.1 N was generated and applied. This is possible because the force to current relationship of the coils is known. The identified transfer function is given in Equation (20) and the identified parameters are as follows: $m = 0.090$ kg, which is -0.0035 kg of the actual measured motional mass, the damping coefficient $c = 9.98$ Ns/m, and the spring coefficient, $k_s = 1685$ N/m, which, is in close agreement with the stiffness measurement. The transfer function fit was 94%. The natural frequency, ω_n , of the CEDAPS can be calculated based on Equation (21) and is found to be 21.78 Hz, which is close to the theoretical value of 23.29 Hz from FEA. The system identification was repeated when the CEDAPS was driven by the micro coil. The identified values were $m = 0.091$ kg, $c = 10.053$ Ns/m, and $k_s = 1701$ N/m with a fitting of 91%, and natural frequency was calculated to be 21.76 Hz, and as expected, they are

similar. The relatively high damping, c , makes the CEDAPS less susceptible to flexure vibrations (ringing) and external disturbances. This is obtained for free when using such an electromagnetic actuator.

$$\frac{X(s)}{F(s)} = \frac{11.11}{s^2 + 110.9s + 18720} \tag{20}$$

$$\omega_n = \frac{1}{2\pi} \sqrt{\frac{k}{m}} \tag{21}$$

Figure 8 shows the Bode plot of the displacement of the CEDAPS concerning the applied force.

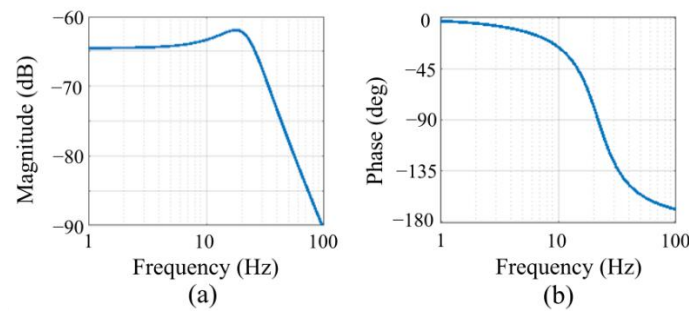


Figure 8. Bode plot of displacement of the macro coil with respect to the applied force. (a) Gain; (b) Phase.

4.2. Tracking of Sinusoidal Reference

Usually, for nanopositioning, the frequency is below 10 Hz and that is also for sub-millimeter displacement. The performance of the CEDAPS was investigated by tracking a 0.5 mm sinusoidal reference with a frequency of 1 Hz, 5 Hz, and 10 Hz, as shown in Figure 9. For the 5 Hz and 10 Hz experiments, the K_{p_M} of the macro coil PID was increased to 120 and 180 respectively, while all the other parameters remained unchanged to compensate for the phase lag, which increases with frequency.

For millimeter range sinusoidal tracking, signals of amplitudes 1 mm, 2.5 mm, and 5 mm at 1 Hz were investigated. The results are shown in Figure 10.

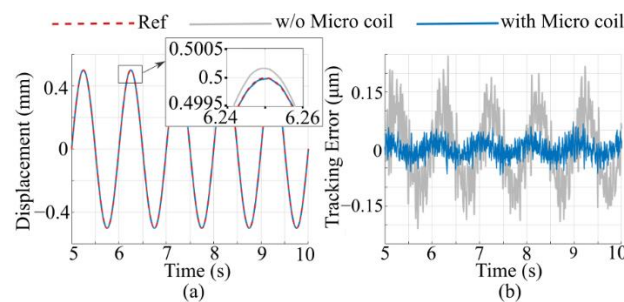


Figure 9. Cont.

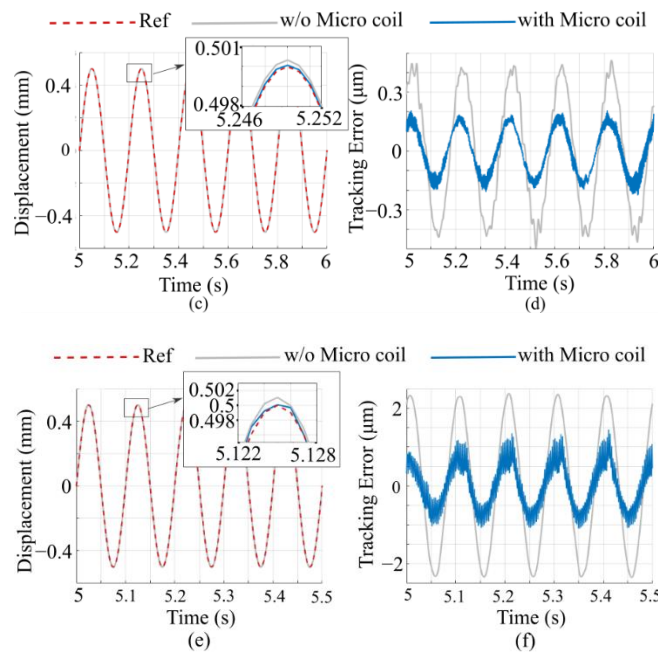


Figure 9. Sinusoidal tracking performance of 0.5 mm amplitude (a) At 1 Hz; (b) Amplitude error under 1 Hz; (c) At 5 Hz; (d) Amplitude error under 5 Hz; (e) At 10 Hz; (f) Amplitude error under 10 Hz.

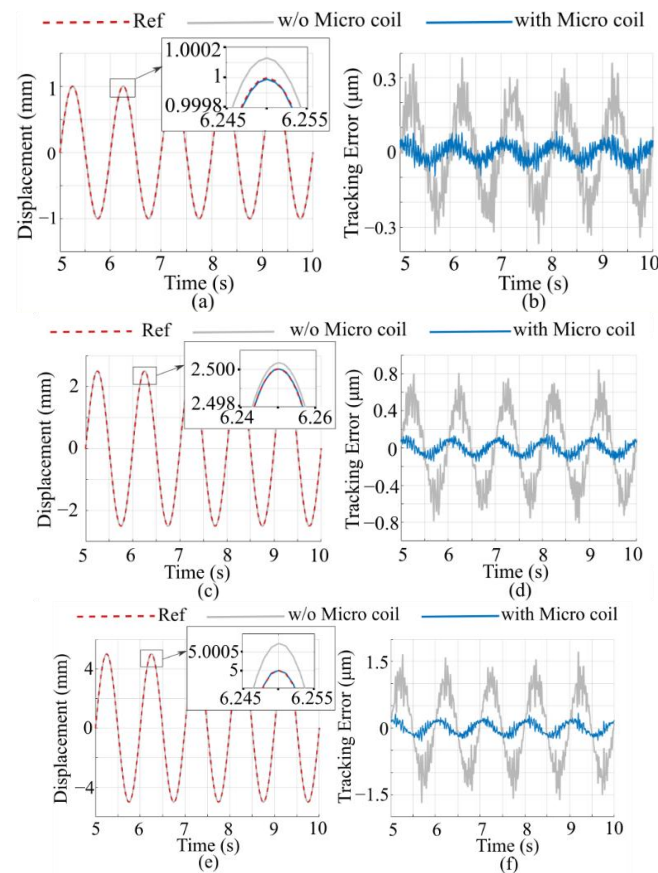


Figure 10. (a) Tracking of 1 mm 1 Hz sinusoidal reference; (b) Error amplitude for 1 mm 1 Hz tracking; (c) Tracking of 2.5 mm 1 Hz sinusoidal reference; (d) Error amplitude for 2.5 mm 1 Hz tracking; (e) Tracking of 5 mm 1 Hz sinusoidal reference; (f) Error amplitude for 5 mm 1 Hz tracking.

The sinusoidal tracking results are summarized in Table 2. The RMSE and MAXE are used as performance indices and are defined as:

$$RMSE = \sqrt{\left(\sum_{i=1}^N e_i^2\right) / N} \tag{22}$$

and

$$MAXE = \max(|e_i|) \tag{23}$$

where e_i is the tracking error.

Table 2. RMSE and MAXE error with and without the micro-coil.

Stroke (mm)	Freq. (Hz)	Macro		Macro—Micro	
		RMSE (μm)	MAXE (μm)	RMSE (μm)	MAXE (μm)
0.5	1	0.091	0.261	0.021 (76.5%)	0.077 (70.3%)
	5	0.302	0.510	0.119 (60.3%)	0.298 (52.1%)
	10	1.354	1.992	0.647 (52.2%)	0.963 (51.6%)
1		0.162	0.384	0.030 (81.2%)	0.105 (63.3%)
2.5	1	0.390	0.853	0.066 (83.2%)	0.188 (67.2%)
5		0.779	1.768	0.128 (83.5%)	0.349 (69.1%)

Percentage improvements with the micro coil are indicated in brackets.

The results for the macro-micro combination show sub-micrometer tracking errors across the range.

4.3. Random Path Tracking

In real-world use, the trajectories will rarely be purely sinusoidal. To this end, a random path, as shown in Figure 11, was used to test the performance of the proposed actuator and controller. The RMSE was 0.1247 μm with the macro coil actuator and 0.0417 μm with the macro and micro coil combination. The MAXE also showed similar improvement. The macro coil had a MAXE of 0.6913 μm while the macro and micro coil combination had 0.2492 μm.

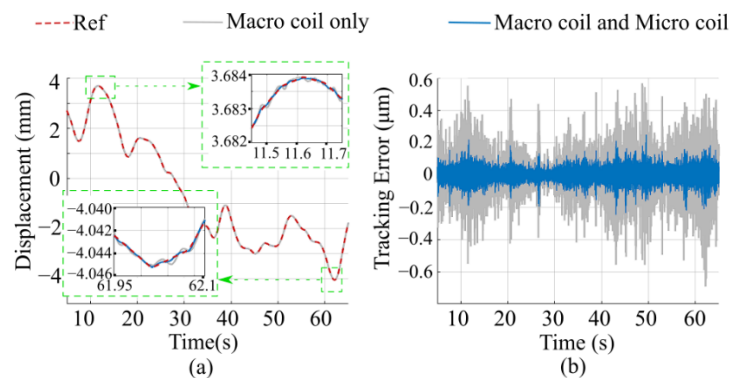


Figure 11. Random trajectory tracking performance. (a) Displacement; (b) Error.

4.4. Step Response

The RGH240x series of linear incremental encoders have a maximum tracking velocity of 0.0625 m/s, and accordingly, the 5 mm step signal was modified to follow a 0.0625 m/s ramp. The tracking performance is shown in Figure 12. The main band is about ± 40 nm for the macro coil and ± 10 nm for the macro-micro configuration. The red and orange lines are the low pass filtered displacement, and it can be seen that with the micro coil, the final positioning error lies within ± 5 nm. This also shows that the micro coil has enough force to correct the holding position error of the macro coil.

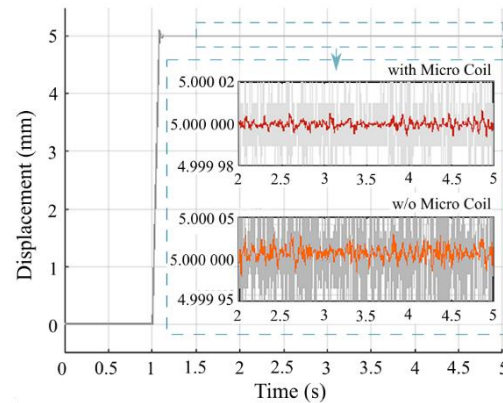


Figure 12. 5 mm step response with and without the micro coil. The solid line shows tracking with a conservative low pass filter.

4.5. Resolution

The resolution of the CEDAPS under an open loop when driven by the macro coil is 1.04 μm and 20 nm for the micro coil, both of which are in line with the theoretical figures. Under the proposed control scheme, the resolution under the macro coil is 50 nm, and it is 10 nm under the macro-micro combination as shown in Figure 13.

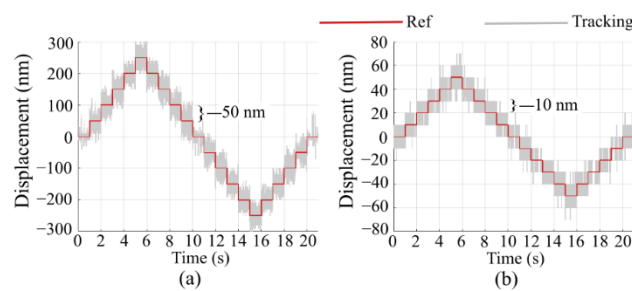


Figure 13. Closed loop resolution with macro coil turned on. (a) Without micro coil; (b) With micro coil enabled.

4.6. Thermal Analysis

The temperature rise and fall of the coils and the head (w.r.t. Figure 3) together with the open loop displacements are shown in Figure 14 when 0.25 A was applied continuously to the macro coil and 0.5 A to the micro-coil for a duration of 1 h, followed by one hour without current. The CEDAPS was mounted on thick polystyrene foam to prevent heat from escaping by conduction. As shown in Figure 14a, these currents cause an initial open-loop displacement of +2.272 mm, which increases by 4.4 μm over the course of one hour, owing primarily to thermal expansion. Meanwhile, the temperature rose by 2.5 $^{\circ}\text{C}$ for the coils and 2.25 $^{\circ}\text{C}$ for the head as shown in Figure 14c. The first thermal time constant for the coils is 370 s, and 776 s for the head during the heating phase. The same can be seen during the cooling phase, as shown in Figure 14b when the current is removed. In actual

application, the bobbin will be in constant motion, which will enhance heat dissipation through forced air cooling.

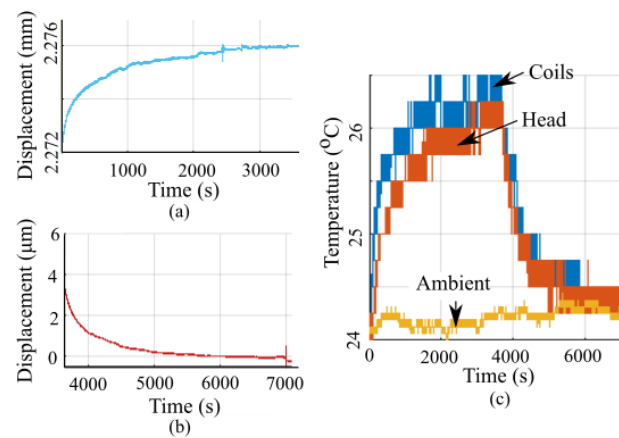


Figure 14. (a) Change in position due to coil currents; (b) change in position when cooling; (c) Temperature of the coils, head and ambient.

5. Discussion and Comparison with Other Works

5.1. Discussion of the Results

The stiffness model of the flexure agrees within 3.1% of that obtained by FEA, and the resulting assembly is within 10% of the FEA value due mostly to small manufacturing imperfections. The resulting stiffness of the assembly is 1650 N/m. The assembly is also compact, has an adequate safety factor of 2.05, and has a natural frequency of 21.78 Hz. The averaged indicative force constant of the macro coil is 13.5 N/A which is within 9% of the FEA simulation and 7% of the theoretical value. The micro coil has a force constant of 0.5 N/A which is within 11% of the FEA and 13% of the theoretically calculated force. These discrepancies can be due to minute assembly errors in the actuator, especially with respect to the placement of the magnets.

The tracking performances were obtained by removing as much non-linearity as possible from the system. The hysteresis in the forces must be accounted for. With this, the tracking RMSE and MAXE can be orders of magnitude higher as opposed to when this force imbalance is countered. Another source of non-ideal behavior is the zero error and deviation from the ideal transconductance of the current drives. Wire-induced disturbances mostly increase stiffness and damping, especially when small forces are required. These must also be accounted for in the design of nanopositioning platforms with moving coil actuators.

The heat generated by the coils depends on the root mean square (RMS) current, and as long as it is less than one Ampere, the heat generated is not excessive, since the square of the numbers between zero and one is less than the number itself. This corresponded to a temperature rise of less than 2.5 °C after one hour of continuous use. Also, the change in displacement due to thermal expansion is in the micrometer range and occurs slowly, which is readily compensated with the position feedback system.

The macro-micro actuation combination showed a 52% to 83% reduction in RMSE and a 41% to 80% reduction in MAXE over macro actuation alone for tracking sinusoidal trajectories. For a random path, the RMSE reduction was 66% and 64% from MAXE. Additionally, the resolution showed a fivefold improvement from 50 nm to 10 nm, which can also be seen in the 5 mm step tracking. Based on these results, it is evident that a dual coil setup is superior.

5.2. Comparison with Other Works

Recently, a VCM-driven annular flexure guide positioning stage (AFPS) employing state-of-the-art flexure design, a 20-bit DAC, controller hardware with 10 kHz sampling, and a better performance VCM with a K_f of around 24 N/A was proposed in [21]. A

similar feed-forward controller and a PID control were utilized. However, no compensation blocks were used. This present work compares favorably to it, as can be seen in Table 3 for sinusoidal trajectory tracking. It can also be seen that as the amplitude becomes larger, the CEDAPS performs better even without the micro coil. On the resolution side, the macro-micro combination is two times higher. Obviously, on the structural side, their work outperforms this one by having a higher natural frequency due to the inherent stiffness of using two annular flexures.

Table 3. Sinusoidal tracking performance comparison with [21].

Freq. (Hz)	Dis. (mm)	% Improvement by This Work			
		Macro		Macro—Micro	
		RMSE	MAXE	RMSE	MAXE
5	0.5	44.1	46.2	78.0	68.6
10		19.6	18.1	61.5	60.4
1	1	22.1	35.4	85.6	82.3
1	5	49.4	33.2	91.7	86.8

This work also compares favorably against other positioning systems employing VCM and flexure hinges, as can be seen in Table 4.

Table 4. Comparison with previous work.

Ref.	Stroke (mm)	Resolution		Natural Frequency (Hz)
		Value (nm)	Percentage of Stroke (%)	
[3]	10	20	0.0002	25
[43]	11	250	0.0023	23.4
[44]	11	200	0.0018	29.3
[34]	10	20	0.0002	30
[45]	7.5	20,000	0.27	8.02
[46]	50	100	0.0002	86
[47]	2.13	250	0.0117	43.7
[48]	2	6000	0.3	32.96
[49]	2	10	0.0005	57.1
[21]	10	20	0.0002	38.99
This work	10	10	0.0001	21.78

Compared with the work of [33], their macro coil has a range of 34.7 μm and a resolution of 2 μm and their micro coil has a 2 nm resolution and a 34.7 nm range. However, no combined resolution and tracking performance were provided. If we assume their system shows a 2 nm resolution for the 34.7 μm stroke, this gives a ratio of resolution to stroke of 0.0058%, which is 58x lower than this present work (0.0001%).

As further work, a more sophisticated controller is under development that can self-adjust for the non-ideal behaviors of the various electrical subsystems of the positioning platform.

6. Conclusions

This work presented the design and experimental validation of a novel electromagnetic dual coil actuator positioning system that has a range of ± 5 mm and a resolution of 10 nm. The actuators are mounted in parallel and only one mechanical positioning stage is used.

A method for calculating the expected open loop resolution and a means of designing a suitable Lorentz's force actuator was also presented. These not only produce a coil with a suitable force constant to maximize resolution but also reduce the heat generated by the coil and also by the linear current drives. The non-ideal behaviors of the positioning subsystems have also been presented and with these, a suitable controller has been presented. The performance of the resulting macro-micro coil actuator was evaluated, and the experimental results show the dual coil setup has superior tracking performance over the single coil setup. Additionally, the tracking performance compares favorably with other recently published works.

Author Contributions: Conceptualization, B.J.G. and Q.Z.; Data curation, B.J.G.; Formal analysis, B.J.G.; Funding acquisition, W.D.; Investigation, B.J.G.; Methodology, B.J.G.; Project administration, W.D.; Resources, W.D.; Software, B.J.G.; Supervision, W.D.; Validation, B.J.G. and Q.Z.; Visualization, B.J.G.; Writing—original draft, B.J.G.; Writing—review & editing, Q.Z. and W.D. All authors have read and agreed to the published version of the manuscript.

Funding: This research was funded by the National Key Research and Development Program of China (Grant No. 2018YFE0206900).

Data Availability Statement: Data sharing is not applicable.

Conflicts of Interest: The authors declare no conflict of interest.

References

1. Teo, T.J.; Bui, V.P.; Yang, G.; Chen, I.-M. Millimeters-Stroke Nanopositioning Actuator with High Positioning and Thermal Stability. *IEEE/ASME Trans. Mechatron.* **2015**, *20*, 2813–2823. [[CrossRef](#)]
2. Shan, G.; Li, Y.; Zhang, L.; Wang, Z.; Zhang, Y.; Qian, J. Contributed Review: Application of Voice Coil Motors in High-Precision Positioning Stages with Large Travel Ranges. *Rev. Sci. Instrum.* **2015**, *86*, 101501. [[CrossRef](#)]
3. Hiemstra, D.B.; Parmar, G.; Awtar, S. Performance Tradeoffs Posed by Moving Magnet Actuators in Flexure-Based Nanopositioning. *IEEE/ASME Trans. Mechatron.* **2014**, *19*, 201–212. [[CrossRef](#)]
4. Devasia, S.; Eleftheriou, E.; Moheimani, S.R. A Survey of Control Issues in Nanopositioning. *IEEE Trans. Control Syst. Technol.* **2007**, *15*, 802–823. [[CrossRef](#)]
5. Makarovic, J. *Lightweight Positioning: Design and Optimization of an Actuator with Two Controlled Degrees of Freedom*; Citeseer: Princeton, NJ, USA, 2006. [[CrossRef](#)]
6. Christiansen, B.; Maurer, H.; Zirn, O. Optimal Control of a Voice-Coil-Motor with Coulombic Friction. In Proceedings of the 2008 47th IEEE Conference on Decision and Control, Cancun, Mexico, 9–11 December 2008; pp. 1557–1562.
7. Lin, C.-J.; Yau, H.-T.; Tian, Y.-C. Identification and Compensation of Nonlinear Friction Characteristics and Precision Control for a Linear Motor Stage. *IEEE/ASME Trans. Mechatron.* **2012**, *18*, 1385–1396. [[CrossRef](#)]
8. Takrouri, M.; Dhaouadi, R. ADALINE-Based Friction Identification of a Linear Voice Coil DC Motor. In Proceedings of the 2016 American Control Conference (ACC), Boston, MA, USA, 6–8 July 2016; pp. 3062–3068. [[CrossRef](#)]
9. Butt, H.U.; Waleed, D.; Dhaouadi, R. Friction Estimation of a Linear Voice Coil Motor Using Robust State Space Sinusoidal Reference Tracking. In Proceedings of the 2018 11th International Symposium on Mechatronics and Its Applications (ISMA), Sharjah, United Arab Emirates, 4–6 March 2018; pp. 1–6. [[CrossRef](#)]
10. Kim, W.; Trumper, D.L.; Lang, J.H. Modeling and Vector Control of Planar Magnetic Levitator. *IEEE Trans. Ind. Appl.* **1998**, *34*, 1254–1262. [[CrossRef](#)]
11. Choi, Y.-M.; Gweon, D.-G. A High-Precision Dual-Servo Stage Using Halbach Linear Active Magnetic Bearings. *IEEE/ASME Trans. Mechatron.* **2011**, *16*, 925–931. [[CrossRef](#)]
12. Zhu, H.; Teo, T.J.; Pang, C.K. Magnetically Levitated Parallel Actuated Dual-Stage (Maglev-PAD) System for Six-Axis Precision Positioning. *IEEE/ASME Trans. Mechatron.* **2019**, *24*, 1829–1838. [[CrossRef](#)]
13. Gao, Q.; Chen, W.; Lu, L.; Huo, D.; Cheng, K. Aerostatic Bearings Design and Analysis with the Application to Precision Engineering: State-of-the-Art and Future Perspectives. *Tribol. Int.* **2019**, *135*, 1–17. [[CrossRef](#)]
14. Tan, K.K.; Huang, S.; Liang, W.; Al Mamun, A.; Koh, E.K.; Zhou, H. Development of a Spherical Air Bearing Positioning System. *IEEE Trans. Ind. Electron.* **2011**, *59*, 3501–3509. [[CrossRef](#)]
15. Howell, L.L. Compliant Mechanisms. In *21st Century Kinematics*; Springer: Berlin/Heidelberg, Germany, 2013; pp. 189–216.
16. Teo, T.J.; Chen, I.-M.; Yang, G.; Lin, W. Magnetic Field Modeling of a Dual-Magnet Configuration. *J. Appl. Phys.* **2007**, *102*, 074924. [[CrossRef](#)]
17. Zhu, H.; Teo, T.J.; Pang, C.K. Analytical Model-Based Multiphysics Optimization of a Nanopositioning Electromagnetic Actuator. *IEEE Trans. Ind. Electron.* **2018**, *65*, 478–487. [[CrossRef](#)]
18. Leung, C.; Lu, Z.; Esfandiari, N.; Casper, R.F.; Sun, Y. Automated Sperm Immobilization for Intracytoplasmic Sperm Injection. *IEEE Trans. Biomed. Eng.* **2010**, *58*, 935–942. [[CrossRef](#)] [[PubMed](#)]

19. Hey, J.; Teo, T.J.; Bui, V.P.; Yang, G.; Martinez-Botas, R. Electromagnetic Actuator Design Analysis Using a Two-Stage Optimization Method with Coarse–Fine Model Output Space Mapping. *IEEE Trans. Ind. Electron.* **2014**, *61*, 5453–5464. [[CrossRef](#)]
20. Probst, M.; Fluckiger, M.; Pané, S.; Ergeneman, O.; Nagy, Z.; Nelson, B.J. Manufacturing of a Hybrid Acoustic Transmitter Using an Advanced Microassembly System. *IEEE Trans. Ind. Electron.* **2009**, *56*, 2657–2666. [[CrossRef](#)]
21. Yang, M.; Zhang, C.; Huang, X.; Chen, S.-L.; Yang, G. A Long Stroke Nanopositioning Stage with Annular Flexure Guides. *IEEE/ASME Trans. Mechatron.* **2021**, *27*, 1570–1581. [[CrossRef](#)]
22. Mori, K.; Munemoto, T.; Otsuki, H.; Yamaguchi, Y.; Akagi, K. A Dual-Stage Magnetic Disk Drive Actuator Using a Piezoelectric Device for a High Track Density. *IEEE Trans. Magn.* **1991**, *27*, 5298–5300. [[CrossRef](#)]
23. Chan, K.W.; Liao, W. Precision Positioning of Hard Disk Drives Using Piezoelectric Actuators with Passive Damping. In Proceedings of the 2006 IEEE International Conference on Mechatronics and Automation, Luoyang, China, 25–28 June 2006; pp. 1269–1274. [[CrossRef](#)]
24. Liu, Y.-T.; Fung, R.-F.; Wang, C.-C. Precision Position Control Using Combined Piezo-VCM Actuators. *Precis. Eng.* **2005**, *29*, 411–422. [[CrossRef](#)]
25. Dong, W.; Tang, J.; ElDeeb, Y. Design of a Linear-Motion Dual-Stage Actuation System for Precision Control. *Smart Mater. Struct.* **2009**, *18*, 095035. [[CrossRef](#)]
26. Xu, Q. Design and Development of a Flexure-Based Dual-Stage Nanopositioning System with Minimum Interference Behavior. *IEEE Trans. Autom. Sci. Eng.* **2012**, *9*, 554–563. [[CrossRef](#)]
27. Ito, S.; Steininger, J.; Schitter, G. Low-Stiffness Dual Stage Actuator for Long Range Positioning with Nanometer Resolution. *Mechatronics* **2015**, *29*, 46–56. [[CrossRef](#)]
28. Jiang, Y.; Zhu, Y.; Yang, K.; Hu, C.; Yu, D. A Data-Driven Iterative Decoupling Feedforward Control Strategy with Application to an Ultraprecision Motion Stage. *IEEE Trans. Ind. Electron.* **2014**, *62*, 620–627. [[CrossRef](#)]
29. Gu, G.-Y.; Zhu, L.-M.; Su, C.-Y.; Ding, H.; Fatikow, S. Modeling and Control of Piezo-Actuated Nanopositioning Stages: A Survey. *IEEE Trans. Autom. Sci. Eng.* **2014**, *13*, 313–332. [[CrossRef](#)]
30. Shinno, H.; Hashizume, H. High Speed Nanometer Positioning Using a Hybrid Linear Motor. *CIRP Ann.* **2001**, *50*, 243–246. [[CrossRef](#)]
31. Seki, K.; Shinohara, Y.; Iwasaki, M.; Chinda, H.; Takahashi, M. Force Controller Design Based on PQ Method for Dual-Stage Actuators in Polishing Machines. In Proceedings of the IECON 2011-37th Annual Conference of the IEEE Industrial Electronics Society, Melbourne, Australia, 7–10 November 2011; pp. 3388–3393. [[CrossRef](#)]
32. Cheung, N.C.; Cheung, B.M. Modelling and Control of a High Speed, Long Travel, Dual Voice Coil Actuator. In Proceedings of the Second International Conference on Power Electronics and Drive Systems, Singapore, 26–29 May 1997; Volume 1, pp. 270–274. [[CrossRef](#)]
33. Yoo, Y.-M.; Kwon, B.-I. A Dual-Servo Type VCM for a Nano-Level Measurement System. *J. Electr. Eng. Technol.* **2007**, *2*, 50–54. [[CrossRef](#)]
34. Zhu, H.; Pang, C.K.; Teo, T.J. A Flexure-Based Parallel Actuation Dual-Stage System for Large-Stroke Nanopositioning. *IEEE Trans. Ind. Electron.* **2017**, *64*, 5553–5563. [[CrossRef](#)]
35. Koseki, Y.; Tanikawa, T.; Koyachi, N.; Arai, T. Kinematic Analysis of a Translational 3-Dof Micro-Parallel Mechanism Using the Matrix Method. *Adv. Robot.* **2002**, *16*, 251–264. [[CrossRef](#)]
36. Donald, B.R.; Levey, C.G.; Paprotny, I. Planar Microassembly by Parallel Actuation of MEMS Microrobots. *J. Microelectromech. Syst.* **2008**, *17*, 789–808. [[CrossRef](#)]
37. Yu, J.; Xie, Y.; Li, Z.; Hao, G. Design and Experimental Testing of an Improved Large-Range Decoupled XY Compliant Parallel Micromanipulator. *J. Mech. Robot.* **2015**, *7*, 044503. [[CrossRef](#)]
38. Pham, H.-H.; Chen, I.-M. Stiffness Modeling of Flexure Parallel Mechanism. *Precis. Eng.* **2005**, *29*, 467–478. [[CrossRef](#)]
39. Xu, Q. New Flexure Parallel-Kinematic Micropositioning System with Large Workspace. *IEEE Trans. Robot.* **2011**, *28*, 478–491. [[CrossRef](#)]
40. Teo, T.J.; Yang, G.; Chen, I.-M. A Flexure-Based Electromagnetic Nanopositioning Actuator with Predictable and Re-Configurable Open-Loop Positioning Resolution. *Precis. Eng.* **2015**, *40*, 249–260. [[CrossRef](#)]
41. Mahnam, A.; Yazdani, H.; Samani, M.M. Comprehensive Study of Howland Circuit with Non-Ideal Components to Design High Performance Current Pumps. *Measurement* **2016**, *82*, 94–104. [[CrossRef](#)]
42. Lee, H.S.; Tomizuka, M. Robust Motion Controller Design for High-Accuracy Positioning Systems. *IEEE Trans. Ind. Electron.* **1996**, *43*, 48–55. [[CrossRef](#)]
43. Xu, Q. Design, Testing and Precision Control of a Novel Long-Stroke Flexure Micropositioning System. *Mech. Mach. Theory* **2013**, *70*, 209–224. [[CrossRef](#)]
44. Xu, Q. Design and Development of a Compact Flexure-Based Xy Precision Positioning System with Centimeter Range. *IEEE Trans. Ind. Electron.* **2013**, *61*, 893–903. [[CrossRef](#)]
45. Shewale, M.S.; Razban, A.; Deshmukh, S.P.; Mulik, S.; Zambare, H.B. Design and Experimental Validation of Voice Coil Motor for High Precision Applications. In Proceedings of the 2018 3rd International Conference for Convergence in Technology (I2CT), Pune, India, 6–8 April 2018; pp. 1–6. [[CrossRef](#)]
46. Roy, N.K.; Cullinan, M.A. Design and Characterization of a Two-Axis, Flexure-Based Nanopositioning Stage with 50 Mm Travel and Reduced Higher Order Modes. *Precis. Eng.* **2018**, *53*, 236–247. [[CrossRef](#)]

47. Cai, K.; Tian, Y.; Liu, X.; Zhang, D.; Shang, J.; Shirinzadeh, B. Development and Control Methodologies for 2-DOF Micro/Nano Positioning Stage with High out-of-Plane Payload Capacity. *Robot. Comput. Integr. Manuf.* **2019**, *56*, 95–105. [[CrossRef](#)]
48. Lin, R.; Li, Y.; Zhang, Y.; Wang, T.; Wang, Z.; Song, Z.; Dou, Z.; Qian, J. Design of A Flexure-Based Mixed-Kinematic XY High-Precision Positioning Platform with Large Range. *Mech. Mach. Theory* **2019**, *142*, 103609. [[CrossRef](#)]
49. Liu, Y.; Zhang, Z. A Large Range Compliant XY Nano-Manipulator with Active Parasitic Rotation Rejection. *Precis. Eng.* **2021**, *72*, 640–652. [[CrossRef](#)]

Disclaimer/Publisher's Note: The statements, opinions and data contained in all publications are solely those of the individual author(s) and contributor(s) and not of MDPI and/or the editor(s). MDPI and/or the editor(s) disclaim responsibility for any injury to people or property resulting from any ideas, methods, instructions or products referred to in the content.